

# Chemical Science

Accepted Manuscript

This article can be cited before page numbers have been issued, to do this please use: H. Wang, J. Zong, S. Wei, M. Li, X. Sun, L. Ye, J. Huang, J. Li, Y. Liu and T. Ma, *Chem. Sci.*, 2026, DOI: 10.1039/D6SC01887D.



This is an Accepted Manuscript, which has been through the Royal Society of Chemistry peer review process and has been accepted for publication.

Accepted Manuscripts are published online shortly after acceptance, before technical editing, formatting and proof reading. Using this free service, authors can make their results available to the community, in citable form, before we publish the edited article. We will replace this Accepted Manuscript with the edited and formatted Advance Article as soon as it is available.

You can find more information about Accepted Manuscripts in the [Information for Authors](#).

Please note that technical editing may introduce minor changes to the text and/or graphics, which may alter content. The journal's standard [Terms & Conditions](#) and the [Ethical guidelines](#) still apply. In no event shall the Royal Society of Chemistry be held responsible for any errors or omissions in this Accepted Manuscript or any consequences arising from the use of any information it contains.

## ARTICLE

**Synchronizing O<sub>2</sub> Adsorption and Proton-Coupled Electron Transfer in Carboxylated Quinoline-Linked Covalent Organic Frameworks to Boost Photocatalytic H<sub>2</sub>O<sub>2</sub> Production**Hao Wang,<sup>a</sup> Junjiang Zong,<sup>a</sup> Shiyuan Wei,<sup>a</sup> Meng Li,<sup>a</sup> Xiaodong Sun,<sup>c</sup> Liqun Ye,<sup>d</sup> Jianhan Huang,<sup>\*a</sup> Jiawei Li,<sup>\*a</sup> You-Nian Liu<sup>a</sup> and Tianyi Ma<sup>b</sup>Received 00th January 20xx,  
Accepted 00th January 20xx

DOI: 10.1039/x0xx00000x

Covalent organic frameworks (COFs) have great potential for photocatalytic H<sub>2</sub>O<sub>2</sub> production, but they are frequently limited by the incompatibility between the thermodynamic O<sub>2</sub> adsorption and the kinetic proton-coupled electron transfer (PCET). The precise design and facile construction of a coordinated microenvironment that integrates “strong O<sub>2</sub> adsorption-rapid PCET” in a single COF remains a great challenge. Herein, for the first time, we developed a de novo construction strategy and successfully synthesized carboxylated quinoline-linked QL-TTB-COF. The quinoline rings reshape the local electronic structure at the active dipyrridyl N sites, significantly strengthening Yeager-type side adsorption of O<sub>2</sub> and sharply boosting H<sub>2</sub>O<sub>2</sub> production via one-step 2e<sup>-</sup> oxygen reduction reaction. Meanwhile, the introduced -COOH not only improves the hydrophilicity of the pore channels but also serves as the proton reservoir, accelerating the overall reaction kinetics by establishing proton transfer networks. In particular, the dipyrridyl and -COOH trigger the 4e<sup>-</sup> water oxidation reaction, offering additional O<sub>2</sub> and protons for H<sub>2</sub>O<sub>2</sub> production. Benefiting from the synergistic “strong O<sub>2</sub> adsorption-rapid PCET” mechanism, QL-TTB-COF achieves a remarkable H<sub>2</sub>O<sub>2</sub> yield rate of 7848 μmol g<sup>-1</sup> h<sup>-1</sup>, and it ranks among the highest levels of the COF-based photocatalysts. This work highlights the significance of precisely controlling the thermodynamic O<sub>2</sub> adsorption and the kinetic proton transfer at the molecular level of the COF-based photocatalysts for H<sub>2</sub>O<sub>2</sub> production.

**Introduction**

Utilizing solar energy to drive oxygen (O<sub>2</sub>) reduction for hydrogen peroxide (H<sub>2</sub>O<sub>2</sub>) production represents a sustainable artificial photosynthesis strategy.<sup>1</sup> Essentially, it stores light energy in chemical bonds via the O<sub>2</sub> + 2H<sup>+</sup> + 2e<sup>-</sup> → H<sub>2</sub>O<sub>2</sub> reaction (2e<sup>-</sup> ORR).<sup>2</sup> The overall efficiency of 2e<sup>-</sup> ORR typically depends on the synergistic supply capability of three reactant species: gas-phase O<sub>2</sub>, photo-generated electrons (e<sup>-</sup>), and protons (H<sup>+</sup>).<sup>3,4</sup> However, the current photocatalytic efficiency of H<sub>2</sub>O<sub>2</sub> production remains severely constrained due to the dynamic mismatch in the concerted supply of these species at the active sites. Therefore, it is imperative to establish a specific catalytic microenvironment, which can thermodynamically enable the precise capture and activation of O<sub>2</sub>, and kinetically ensure the rapid and synchronous transfer of e<sup>-</sup> and H<sup>+</sup>.

Covalent organic frameworks (COFs) have emerged as an ideal platform for photocatalytic H<sub>2</sub>O<sub>2</sub> production, owing to their customizable backbone, permanent porosity, and exceptional stability.<sup>5,6</sup> The local electronic structure of the COFs can be readily modulated to promote rapid transfer of photo-generated electrons. However, the interfacial transfer of photo-generated electrons typically occurs at femtosecond to picosecond timescale, while the diffusion-controlled proton transfer lags significantly behind, and this spatiotemporal mismatch often results in kinetically limited proton-coupled electron transfer (PCET).<sup>7,8</sup> It is found that introducing specific functional groups, such as -COOH, -OH and -SO<sub>3</sub>H, to the COFs is effective.<sup>9,10</sup> They can act as proton relays by forming hydrogen-bond networks, effectively reducing the activation energy of proton diffusion and enabling the protons to be promptly transferred to the active sites.<sup>11,12</sup> Nevertheless, the overall reaction rate is still largely restricted by the consistent compatibility between the thermodynamic O<sub>2</sub> adsorption and the rate-determining PCET step,<sup>13,14</sup> which stems from the much lower diffusion of H<sup>+</sup> (~2.39 × 10<sup>-9</sup> m<sup>2</sup> s<sup>-1</sup>, 300 K) than that of O<sub>2</sub> (~1.88 × 10<sup>-5</sup> m<sup>2</sup> s<sup>-1</sup>).<sup>11,15</sup> Furthermore, the inherent hydrophobicity of the COFs backbone creates a substantial proton transfer barrier, thereby forming a “proton-deficient” microenvironment around the active sites.<sup>7,16</sup> In this context, precisely designing and carefully constructing a coordinated microenvironment that integrates “strong O<sub>2</sub> adsorption-rapid PCET” in a single COF remains a great challenge.

For this purpose, for the first time, an ingenious dual regulation strategy targeting both strong O<sub>2</sub> adsorption and rapid transfer of e<sup>-</sup> and H<sup>+</sup> was proposed for the COF photocatalysts. To the best of our

<sup>a</sup> College of Chemistry and Chemical Engineering, Key Laboratory of Micro and Nano Material Interface Science, Central South University, Changsha, 410083, China, E-mail: jianhanhuang@csu.edu.cn; lijawei@csu.edu.cn

<sup>b</sup> Centre for Atomaterials and Nanomanufacturing (CAN), RMIT University, Melbourne, VIC 3000, Australia, E-mail: tianyi.ma@rmit.edu.au

<sup>c</sup> Institute of Clean Energy Chemistry, Key Laboratory for Green Synthesis and Preparative Chemistry of Advanced Materials, College of Chemistry, Liaoning University, Shenyang, 110036, China

<sup>d</sup> College of Materials and Chemical Engineering, Key Laboratory of inorganic nonmetallic crystalline and energy conversion materials, China Three Gorges University, Yichang 443002, China



knowledge, despite extensive research on PCET alone,<sup>7-10, 17-20</sup> studies on O<sub>2</sub> adsorption synergistic PCET remain largely unexplored.<sup>8</sup> Through a facile one-pot solvothermal method, three COFs (TTB-COF, BQ-TTB-COF and QL-TTB-COF, Figure 1a) were comparatively synthesized. It is found that transformation of the imine bonds to quinoline rings not only improves the conjugation degree and chemical stability of the COFs, but also effectively modulates the local electronic structure, promoting Yeager-type side adsorption of O<sub>2</sub> at the dipyriddy N sites and facilitating O<sub>2</sub> reduction for H<sub>2</sub>O<sub>2</sub> production via one-step 2e<sup>-</sup> ORR pathway. Meanwhile, the embedded side-chain -COOH in QL-TTB-COF not only enhances the hydrophilicity of the pore channels, but also provides ample H<sup>+</sup> for the 2e<sup>-</sup> ORR, thereby accelerating the overall reaction kinetics by rapid PCET. Moreover, this precise regulation ignites the 4e<sup>-</sup> water

oxidation reaction (WOR), which offers additional O<sub>2</sub> and H<sup>+</sup> for the 2e<sup>-</sup> ORR. Benefiting from the promotion of O<sub>2</sub> adsorption and the optimization of continuous PCET process, QL-TTB-COF achieves a H<sub>2</sub>O<sub>2</sub> yield rate up to 7848 μmol g<sup>-1</sup> h<sup>-1</sup> in pure water, significantly higher than BQ-TTB-COF (3523 μmol g<sup>-1</sup> h<sup>-1</sup>) and TTB-COF (1444 μmol g<sup>-1</sup> h<sup>-1</sup>), and ranks among the highest levels of the COF-based photocatalysts.

## Results and discussion

### Synthesis and Characterization of the Photocatalysts

The triazine ring is a N-rich and electron-deficient moiety, which is

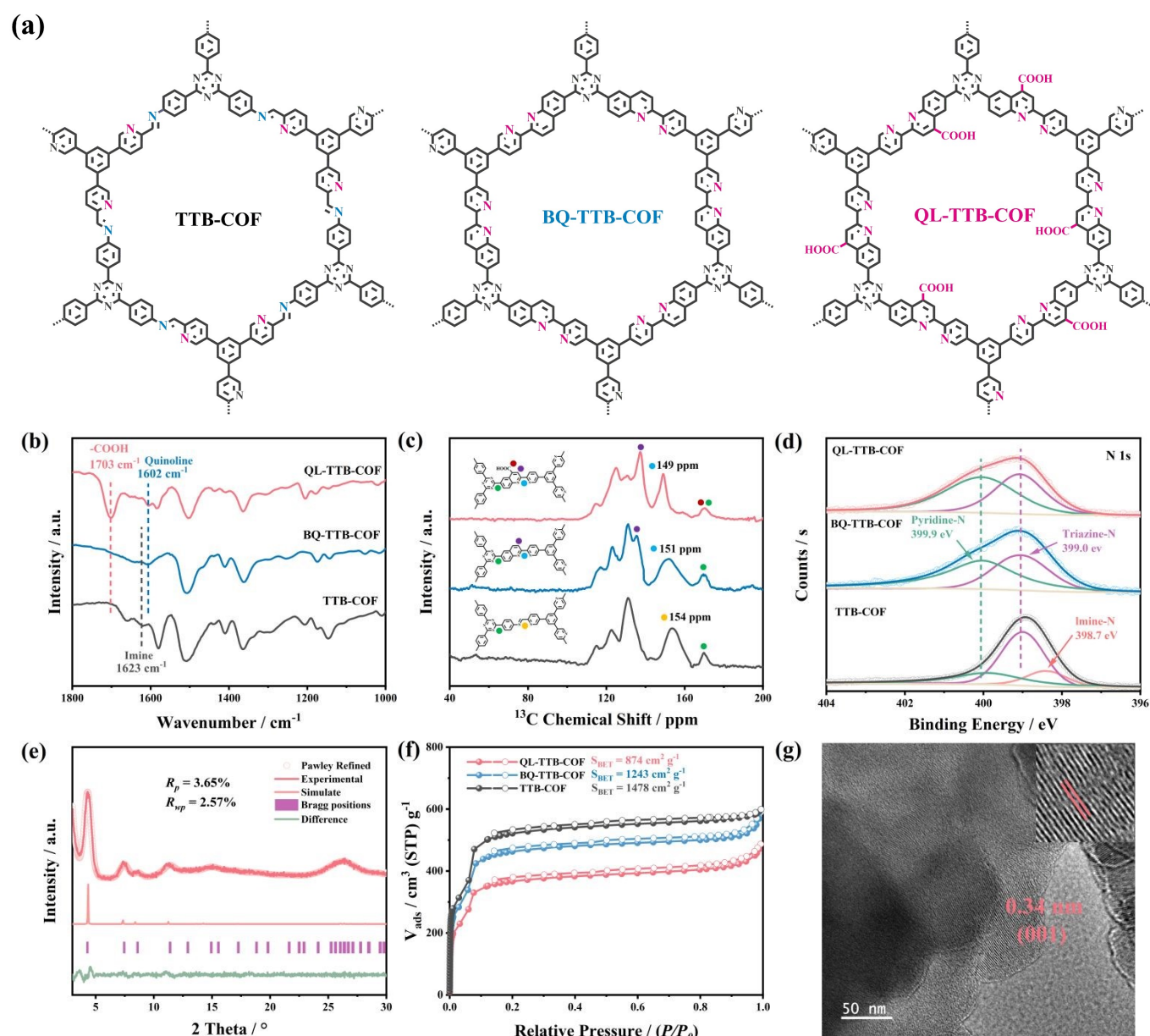


**Figure 1.** (a) Chemical structure of TTB-COF, BQ-TTB-COF and QL-TTB-COF, (b) FT-IR spectra, (c) Solid-state <sup>13</sup>C NMR spectra, (d) N 1s spectra of TTB-COF, BQ-TTB-COF and QL-TTB-COF, (e) PXRD pattern of QL-TTB-COF, (f) N<sub>2</sub> adsorption-desorption isotherms of TTB-COF, BQ-TTB-COF and QL-TTB-COF, (g) TEM image of QL-TTB-COF.



beneficial for light absorption, and it is proven the promising photocatalytic unit.<sup>21</sup> Additionally, the pyridine N of 5,5',5''-(1,3,5-benzenetriyl)tris[2-pyridinecarboxaldehyde] (BTPA) can serve as the active sites for O<sub>2</sub> adsorption.<sup>22</sup> Therefore, TTb-COF was firstly synthesized by a typical Schiff base reaction using 4,4',4''-(1,3,5-triazine-2,4,6-triyl)trianiline (TAPT) and BTPA as the monomers, the formed imine bonds and the adjacent pyridine N may be the active sites for O<sub>2</sub> adsorption and subsequent ORR. Afterwards, by a one-pot three-component reaction, the novel quinoline-linked BQ-TTB-COF was constructed using TAPT and BTPA as the monomers and triethylamine as the vinyl source.<sup>23</sup> It is observed that the imine bonds are transformed to the quinoline rings with the dipyridyl structure. It can be expected that the formed unique dipyridyl N can significantly enhance O<sub>2</sub> adsorption, sharply boosting H<sub>2</sub>O<sub>2</sub> production via one-step 2e<sup>-</sup> ORR. Furthermore, by a three-component Doebner reaction, we introduced side-chain -COOH in BQ-TTB-COF and fabricated the carboxylated quinoline-linked QL-TTB-COF.<sup>24</sup> The induced -COOH is anticipated to form hydrogen-bond transfer networks and provide abundant H<sup>+</sup> for H<sub>2</sub>O<sub>2</sub> production by accelerating the overall reaction kinetics.

The chemical structure of the three COFs was firstly characterized by Fourier transform infrared (FT-IR) spectroscopy. Compared to the imine-linked TTb-COF, the attenuation of C=N stretching at approximately 1623 cm<sup>-1</sup> and the appearance of quinoline rings at around 1602 cm<sup>-1</sup> verify the quinoline-linked BQ-TTB-COF and QL-TTB-COF (Figure 1b and Figure S1).<sup>23</sup> Additionally, the peak at 1703 cm<sup>-1</sup> can be assigned to -COOH in QL-TTB-COF.<sup>24</sup> The solid-state <sup>13</sup>C NMR spectra of TTb-COF exhibit the characteristic imine C at 154

ppm (Figure 1c), while this signal is absent for BQ-TTB-COF and QL-TTB-COF, where those of quinoline rings present at approximately 151 ppm. The characteristic -COOH peak of QL-TTB-COF presents at 168 ppm, overlapping with the triazine peak.<sup>24, 25</sup> X-ray photoelectron spectroscopy (XPS) supported the above conclusions. Figure 1d demonstrates that the imine bonds at 398.7 eV are completely vanished for BQ-TTB-COF and QL-TTB-COF, while a strong pyridine N signal of quinoline rings appears at 399.9 eV, and the conversion of imine bonds to quinoline rings is successful.<sup>25</sup> Additionally, in C 1s spectra of QL-TTB-COF, the characteristic peak at 289.1 eV can be assigned to the side-chain -COOH (Figure S2-S4).<sup>24, 25</sup>

The crystallinity of the photocatalysts was evaluated by powder X-ray diffraction (PXRD). They exhibit similar diffraction patterns and display intense reflections in the low-angle region at 4.1° (Figure 1e and Figure S5-S6).<sup>26, 27</sup> The simulation results indicate that the experimental PXRD data of these COFs closely match the simulated AA stacking model, with Pawley fitting analysis yielding R factors of less than 5% for both unweighted-profile (*R<sub>p</sub>*) and weighted-profile (*R<sub>wp</sub>*). Based on N<sub>2</sub> adsorption-desorption isotherms (Figure 1f), the Brunauer-Emmett-Teller (BET) surface area of TTb-COF, BQ-TTB-COF, and QL-TTB-COF is calculated to be 1478 m<sup>2</sup> g<sup>-1</sup>, 1243 m<sup>2</sup> g<sup>-1</sup>, and 874 m<sup>2</sup> g<sup>-1</sup>, with average pore size of about 2.3 nm, 2.2 nm, and 2.0 nm, respectively (Figure S7). The microstructure of the COFs was characterized using scanning electron microscopy (SEM) and transmission electron microscopy (TEM). The SEM images in Figure S8 reveal that they are irregular nanoparticles. The HR-TEM images in Figure 1g show that crystalline domains with ordered lattice

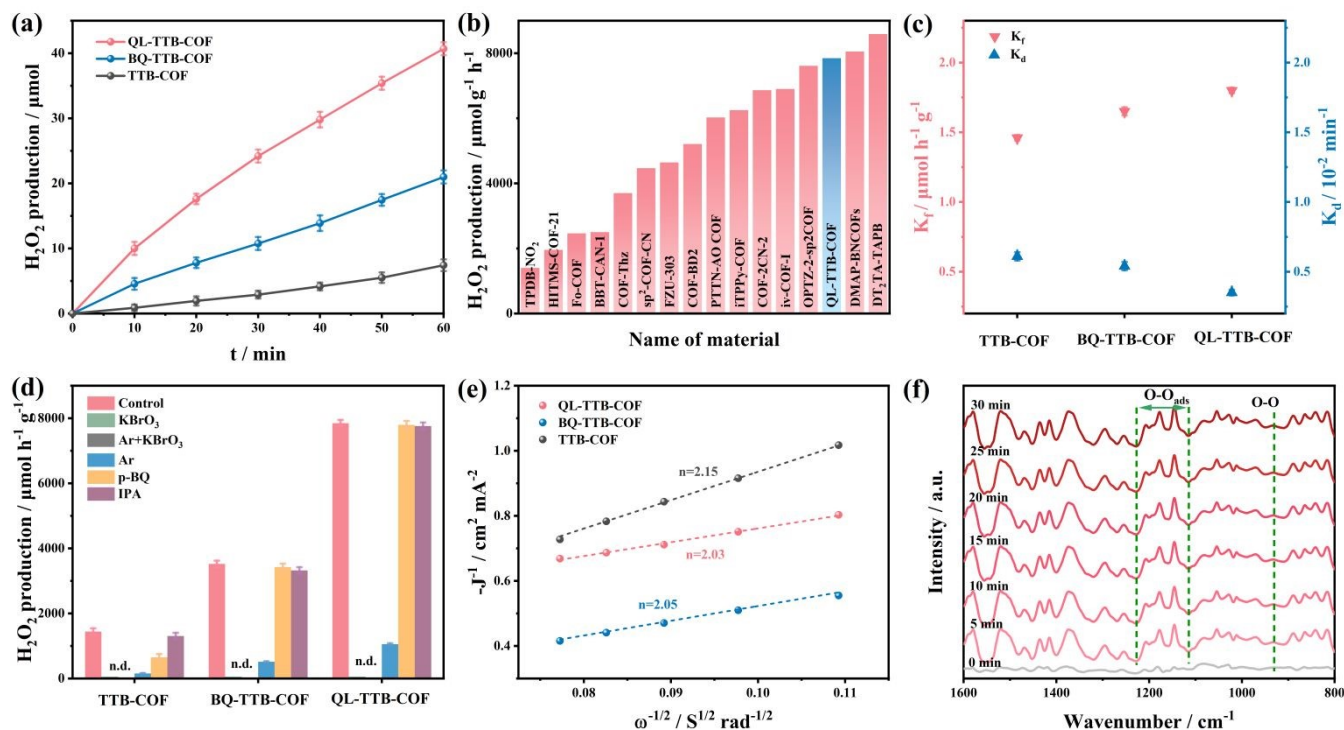


**Figure 2.** (a) Time-dependent H<sub>2</sub>O<sub>2</sub> production of the photocatalysts (5 mg catalyst in 40 mL water, λ > 420 nm Xe lamp), (b) H<sub>2</sub>O<sub>2</sub> production rate of QL-TTB-COF in comparison with other COF-based photocatalysts, (c) K<sub>f</sub> and K<sub>a</sub> of H<sub>2</sub>O<sub>2</sub>, (d) Control experiments, (e) Koutecky–Levich plots by RDE measurements at -1.0 V (vs. Ag/AgCl), (f) In situ DRIFTS spectra QL-TTB-COF.



fringes with an interplanar d-spacing of 0.34 nm, coherent with the QL-TTB-COF interlayer spacing of the simulated pattern (Figure S9-S11).

### Photocatalytic H<sub>2</sub>O<sub>2</sub> Production

The photocatalytic H<sub>2</sub>O<sub>2</sub> production performance of the three COFs was comparatively investigated in pure water without any sacrificial agent under visible-light irradiation (300 W Xe lamp,  $\lambda \geq 420$  nm) at room temperature. The H<sub>2</sub>O<sub>2</sub> amount was determined using potassium iodide colorimetric analysis and the standard curve in Figure S12. As shown in Figure 2a, QL-TTB-COF exhibits almost constant H<sub>2</sub>O<sub>2</sub> production during one-hour operation, with the yield rate of 7848  $\mu\text{mol g}^{-1} \text{h}^{-1}$ , significantly higher than BQ-TTB-COF (3523  $\mu\text{mol g}^{-1} \text{h}^{-1}$ ) and TTB-COF (1444  $\mu\text{mol g}^{-1} \text{h}^{-1}$ ). This enhanced photocatalytic activity is likely attributed to the synergistic integration of the introduced dipyriddy structure and -COOH, which thermodynamically facilitates O<sub>2</sub> adsorption and kinetically accelerates proton transfer, thereby accelerating the rate-determining PCET process. Certainly, this yield rate ranks among the highest levels of the materials in similar applications (Figure 2b and Table S1). To evaluate the light utilization efficiency of QL-TTB-COF in pure water, its apparent quantum yield (AQY) under monochromatic light irradiation at 420 nm is measured to be 8.8% (Figure S13). Additionally, its solar-to-chemical conversion efficiency (SCC) reaches 0.16%, outperforming that of naturally occurring plants ( $\sim 0.10\%$ ).<sup>28</sup> The optimal dosage of QL-TTB-COF is 0.125 mg mL<sup>-1</sup> (Figure S14), and it has high compatibility with various aqueous matrices, including Xiangjiang River water in China, seawater, and tap water (Figure S15).

The generation and decomposition of H<sub>2</sub>O<sub>2</sub> are two competing pathways for H<sub>2</sub>O<sub>2</sub> production, and the photocatalytic decomposition experiments of H<sub>2</sub>O<sub>2</sub> (100  $\mu\text{M L}^{-1}$ ) indicate that QL-TTB-COF displays negligible degradation of H<sub>2</sub>O<sub>2</sub>. After one hour of visible light irradiation, the H<sub>2</sub>O<sub>2</sub> concentration remains above 95% of its initial value (Figure S16), illustrating its continuous generation over its decomposition. Noticeably, by evaluating the generation rate constant ( $K_f$ ) and the decomposition rate constant ( $K_d$ ), Figure 2c displays that QL-TTB-COF has the highest  $K_f$  while the lowest  $K_d$  among the three photocatalysts, indicating that the introduction of -COOH groups does not promote H<sub>2</sub>O<sub>2</sub> adsorption and decomposition. QL-TTB-COF was reused for five cycles without significant deactivation (Figure S17), with its pore structure and chemical composition well preserved (Figure S18), demonstrating the robust durability required for sustained H<sub>2</sub>O<sub>2</sub> production.<sup>5</sup>

### Reaction Pathway for H<sub>2</sub>O<sub>2</sub> Production

A series of control experiments were performed to investigate the reaction pathways for H<sub>2</sub>O<sub>2</sub> production. As shown in Figure 2d, the addition of KBrO<sub>3</sub> (e<sup>-</sup> scavenger) results in nearly undetectable H<sub>2</sub>O<sub>2</sub> for the COFs. In contrast, the incorporation of isopropanol (IPA,  $\cdot\text{OH}$  scavenger) has negligible effect. This indicates that the primary source of H<sub>2</sub>O<sub>2</sub> originates from the 2e<sup>-</sup> ORR, rather than the 2e<sup>-</sup> WOR.<sup>18</sup> Interestingly, the addition of *p*-benzoquinone (*p*-BQ,  $\cdot\text{O}_2^-$  scavenger) sharply reduces H<sub>2</sub>O<sub>2</sub> production for TTB-COF, while those of BQ-TTB-COF and QL-TTB-COF remain largely unaffected, even at high concentrations of *p*-BQ (0.01-0.1 mM, Figure S19). That is to say, for TTB-COF,  $\cdot\text{O}_2^-$  plays a pivotal role as the key intermediate for H<sub>2</sub>O<sub>2</sub> production, and H<sub>2</sub>O<sub>2</sub> is produced according to both one-

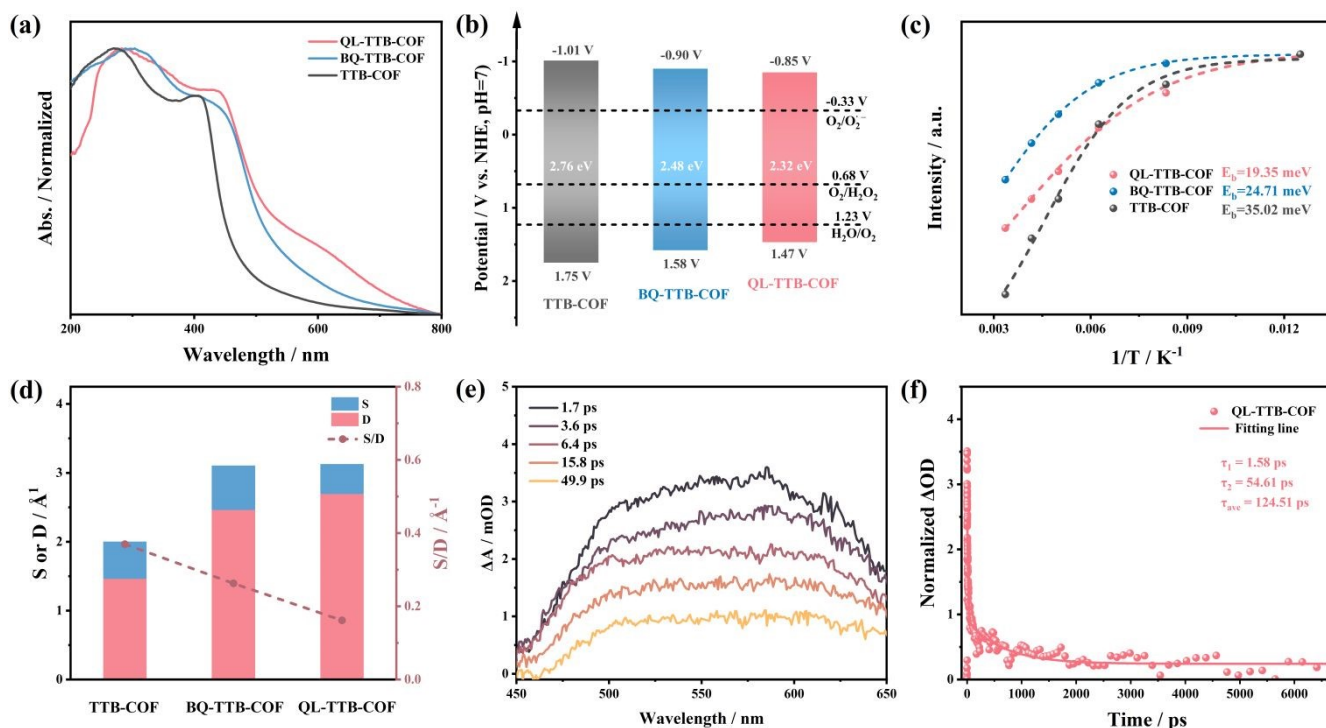


**Figure 3.** (a) Ultraviolet-visible diffuse reflectance spectra, (b) Band structure, (c) Temperature-dependent photoluminescence spectra, (d) Electron-hole distribution, (e) Fs-TAS spectra at different decay time, (f) Decay kinetic curves of QL-TTB-COF.



step  $2e^-$  ORR and two-step  $2e^-$  ORR.<sup>29</sup> This phenomenon may arise from the readily occurring  $O_2$  detachment as the imine N and the pyridine N simultaneously engage in Yeager-type side adsorption. In contrast, the  $H_2O_2$  production on BQ-TTB-COF and QL-TTB-COF does not involve the  $\cdot O_2^-$  species. That is, after the imine bonds were converted to the quinoline rings with dipyridyl structure, the  $O_2$  adsorption is greatly enhanced by Yeager-type, thereby generating  $H_2O_2$  via the one-step  $2e^-$  ORR. Notably, it is seen that  $H_2O_2$  can be detected in Ar-saturated solution, whereas no  $H_2O_2$  is observed in Ar-saturated  $KBrO_3$  solution, manifesting that the photo-generated holes participate in the  $H_2O$  oxidation process via  $4e^-$  WOR, and the produced  $O_2$  and  $H^+$  may facilitate the  $2e^-$  ORR for  $H_2O_2$  production.<sup>8, 18</sup>

The isotope labeling experiments were thereafter conducted using  $^{18}O_2$  and  $H_2^{16}O$  to distinguish the oxygen source for  $H_2O_2$ .  $MnO_2$  was added to degrade the produced  $H_2O_2$  to  $O_2$ , and the released  $O_2$  was analyzed by gas chromatography-mass spectrometry (GC-MS).<sup>30</sup> The results in Figure S20 mean that both of  $^{18}O_2$  and  $^{16}O_2$  are present in the system, meaning that the generated  $H_2O_2$  is originated from both  $2e^-$  ORR and  $4e^-$  WOR.<sup>18</sup> After combining these two peaks,  $^{18}O_2$  and  $^{16}O_2$  account for 92.8% and 7.2% of the total  $H_2O_2$ . That is, the dissolved atmospheric  $O_2$  for  $2e^-$  ORR and in situ generated  $O_2$  based on  $4e^-$  WOR account for 92.8% and 7.2%. Surprisingly, we observe that the contribution of the  $4e^-$  WOR for  $H_2O_2$  production on QL-TTB-COF is much greater than that on BQ-TTB-COF (3.5%) and TTB-COF (1.1%, Table S2). It can be concluded that the introduced -COOH in QL-TTB-COF trigger the efficiency of  $4e^-$  WOR, offering additional  $O_2$  and  $H^+$  for the ORR. Meanwhile, the  $O_2$  evolution in the catalytic system was detected under saturated Ar-saturated  $KBrO_3$  solution (Figure S21), and it is evident that the  $O_2$  evolution capacity of QL-TTB-COF is greatly higher than BQ-TTB-COF and TTB-COF. Furthermore, the analysis of charge density difference is in favor of this conclusion. As compared with the  $H_2O$  molecules on TTB-COF and BQ-TTB-COF, QL-TTB-COF can lose more electrons (Figure S22), suggesting that it has a stronger ability to oxidize  $H_2O$  and produce  $O_2$ .

By the electrochemical analysis on a rotating disk electrode (RDE), the selectivity to the  $2e^-$  ORR was further evaluated. The results in Figure 2e indicate that the electron transfer number for BQ-TTB-COF and QL-TTB-COF is closer to 2 (Figure S23-S25), which is conducive to the  $2e^-$  ORR pathway.<sup>2</sup> The reactive oxygen species in the ORR were further investigated by EPR experiment using 5,5-dimethyl-1-pyrroline-oxide (DMPO) as the spin trapping agent. As shown in Figure S26, TTB-COF exhibits the characteristic six-line peak of DMPO- $\cdot O_2^-$ , whereas BQ-TTB-COF and QL-TTB-COF do not display this peak, confirming that the formation of dipyridyl structure significantly restrains the generation of  $\cdot O_2^-$ . Furthermore, the amount of  $\cdot O_2^-$  in the system was quantitatively determined by nitro blue tetrazolium salt (NBT), a reagent that is specifically captured only by  $\cdot O_2^-$ . As shown in Figure S27, negligible  $\cdot O_2^-$  is detected for BQ-TTB-COF and QL-TTB-COF, further clarifying that  $H_2O_2$  production on BQ-TTB-COF and QL-TTB-COF occurs via one-step  $2e^-$  ORR rather than two-step  $2e^-$  ORR.<sup>22, 31</sup> Noticeably, no characteristic signals of  $\cdot OH$  radicals were detected for the three COFs, ruling out the  $2e^-$  WOR (Figure S28). In situ diffuse reflect infrared Fourier transform (DRIFTS) spectroscopy was carried out and it reveals that QL-TTB-COF

has a strong signal in the range of  $1115-1295\text{ cm}^{-1}$ , which can be assigned to the  $-O-O-$  vibration (Figure 2f). Within 10 min of irradiation, the intensity of this signal remains unchanged and retains thereafter. Additionally, a new vibration at  $910\text{ cm}^{-1}$  is observed for QL-TTB-COF, which should be ascribed to the 1,4-peroxy intermediate, thereby confirming the Yeager-type side adsorption of  $O_2$ .<sup>22, 31</sup>

### Photoelectrochemical Properties and Electronic Structure

Ultraviolet-visible diffuse reflectance spectroscopy of the three COFs in Figure 3a reveals a progressive red shift from TTB-COF to BQ-TTB-COF and to QL-TTB-COF, and the introduced quinoline rings and -COOH should be the main reasons due to the extended conjugation.<sup>32</sup> The optical band gaps of TTB-COF, BQ-TTB-COF, and QL-TTB-COF were determined to be 2.76 eV, 2.48 eV and 2.32 eV, respectively (Figure S29). In addition, the positions of conduction band (CB) and valence band (VB) of the COFs were determined by Mott-Schottky (M-S) electrochemical measurements combined with optical band gap, and their CB and VB potentials were determined (Figure S30-S35) as follows: TTB-COF at  $-1.01\text{ V}$  and  $+1.75\text{ V}$ , BQ-TTB-COF at  $-0.90\text{ V}$  and  $+1.58\text{ V}$ , and QL-TTB-COF at  $-0.85\text{ V}$  and  $+1.47\text{ V}$  (vs. NHE). These values indicate the thermodynamic feasibility of the one-step  $2e^-$  ORR ( $+0.68\text{ V}$  vs. NHE) and the  $4e^-$  WOR ( $+1.23\text{ V}$  vs. NHE) for  $H_2O_2$  production (Figure 3b). In particular, the geometric optimization of the COFs was performed, and the highest occupied molecular orbital (HOMO)-lowest unoccupied molecular orbital (LUMO) energy was calculated (Figure S36). Noticeably, the energy level diagram exhibits similar trends with the measured CB and VB, particularly, it reflects the narrowest band gap of QL-TTB-COF among the three photocatalysts.<sup>18</sup>

The charge dynamics of the COFs were then investigated and the EIS Nyquist plot reveals that QL-TTB-COF owns the lowest charge transfer resistance ( $R_{ct}$ ), implying its highest charge transfer efficiency and greatest mobility capability of photo-generated carriers (Figure S37 and Table S3).<sup>33</sup> Moreover, under visible light irradiation, QL-TTB-COF has rapid photo-current response, confirming its greatest transfer efficiency of photo-generated carriers (Figure S38). Additionally, under visible light irradiation and at the same frequency, QL-TTB-COF has the much lower slope in the Mott-Schottky plot, implying its higher carrier concentration (Figure S39). Meanwhile, the photoluminescence (PL) and time-resolved PL (TRPL) spectroscopy of the COFs were studied and it can be seen that under 342 nm excitation, QL-TTB-COF has much reduced PL emission intensity, manifesting that it can effectively inhibit the recombination of photo-generated electrons and holes (Figure S40).<sup>6, 34</sup> According to the TRPL results (Figure S41), the average lifetime of QL-TTB-COF is 3.19 ns, slightly longer than BQ-TTB-COF (2.97 ns) and much longer than TTB-COF (1.35 ns). The temperature-dependent PL (TD-PL) spectroscopy was thereafter analyzed and the exciton binding energy ( $E_b$ ) was determined. As can be observed in Figure 3c and Figure S42, the  $E_b$  values of TTB-COF, BQ-TTB-COF, and QL-TTB-COF were 35.02 meV, 24.71 meV and 19.35 meV, respectively. The minimum  $E_b$  of QL-TTB-COF implies the highest exciton dissociation efficiency. That is, the conversion of the imine bonds to quinoline rings as well as the introduction of the -COOH on the COFs effectively modulates the local electronic structure. The electron-hole



distribution at excited state was investigated by time-dependent DFT calculations. As shown in Figure 3d and Table S4, the S/D value of QL-TTB-COF is significantly lower than BQ-TTB-COF and TTb-COF, suggesting the rapid separation and transfer of photo-generated carriers.<sup>35</sup> The femtosecond time-resolved absorption (fs-TA) spectroscopy was then conducted (Figure 3e-f and Figure S43), and it is observed that these COFs exhibit positive photo-induced absorption (PIA) bands in 450–650 nm, with the absorption peak around 590 nm. This is attributable to photo-induced electron absorption and persists for duration exceeding microseconds.<sup>23</sup> Particularly, QL-TTB-COF has the strongest ESA absorption, confirming its most effective carrier separation capability. The kinetic fitting results reveal a dual-exponential decay process, characterized by a short lifetime ( $\tau_1$ ) and a long lifetime ( $\tau_2$ ), corresponding to electron trapping and electron transfer kinetics, respectively. According to the kinetic curve, it is seen that QL-TTB-COF has a much longer average lifetime ( $\tau_{avg} = 124.51$  ps) compared to BQ-TTB-COF

( $\tau_{avg} = 62.85$  ps) and TTb-COF ( $\tau_{avg} = 21.97$  ps), indicating the highest exciton dissociation and charge transfer efficiency.

### O<sub>2</sub> Adsorption and Proton Transfer Efficiency

To investigate the different effects of the imine N and dipyriddy N on O<sub>2</sub> adsorption, the O<sub>2</sub> adsorption on the three COFs were evaluated via temperature-programmed O<sub>2</sub> desorption (O<sub>2</sub>-TPD) (Figure 4a). Compared to TTb-COF (119 °C), BQ-TTB-COF and QL-TTB-COF have broad and intense high-temperature desorption peaks (130 °C and 133 °C, respectively). Quantitative analysis demonstrates that the O<sub>2</sub> adsorption capacity of QL-TTB-COF is up to 0.0319 mmol g<sup>-1</sup>, much higher than BQ-TTB-COF (0.0282 mmol g<sup>-1</sup>) and TTb-COF (0.0081 mmol g<sup>-1</sup>). That is, the newly formed dipyriddy structure in BQ-TTB-COF effectively enhances O<sub>2</sub> adsorption, and the induced -COOH in QL-TTB-COF further strengthens the O<sub>2</sub> adsorption by induction effect. Moreover, the electrostatic potential (ESP) simulations

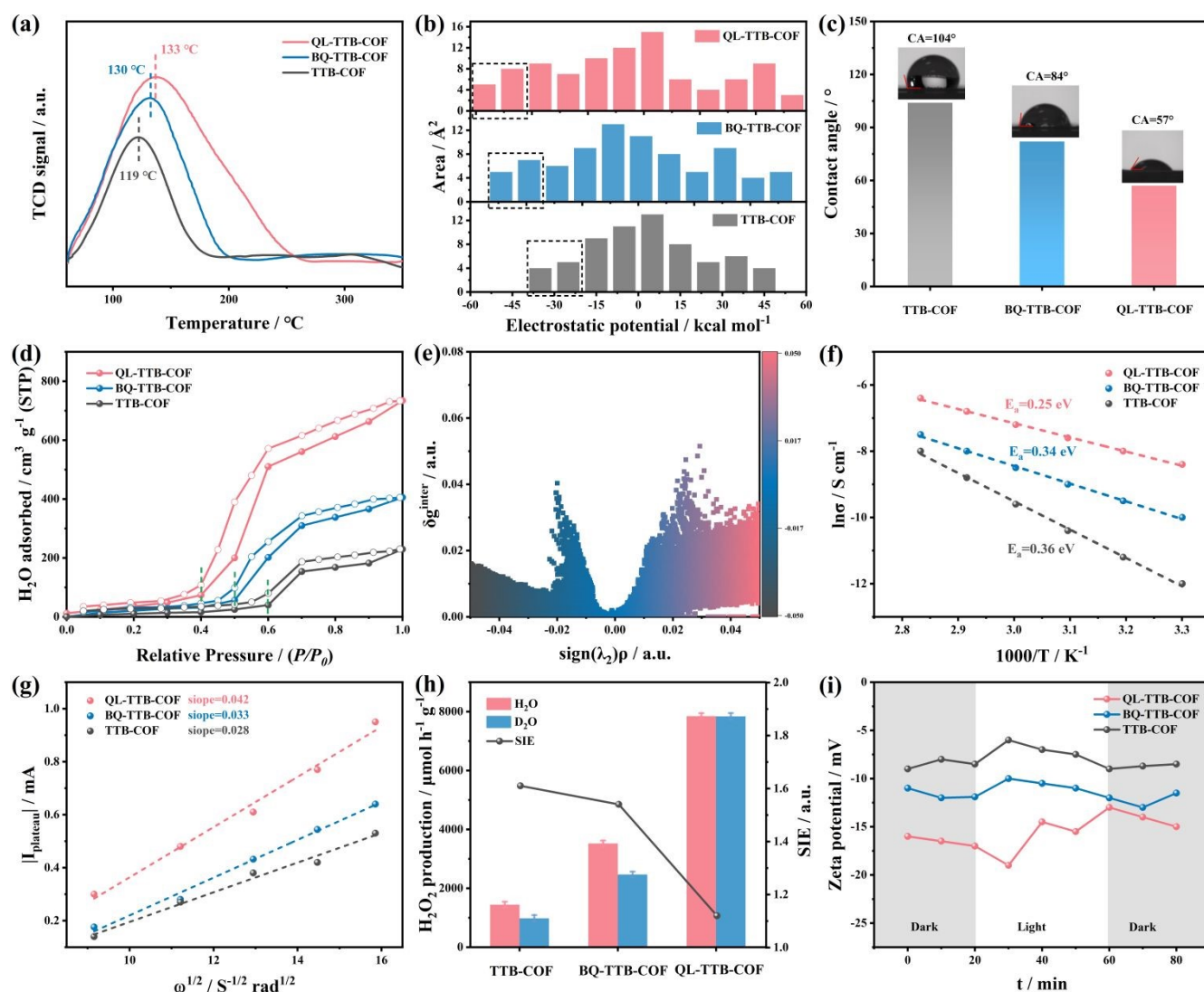


**Figure 4.** (a) O<sub>2</sub>-TPD curves, (b) Quantitative electrostatic potential profiles, (c) Water contact angles, (d) Water vapour desorption isotherms, (e) Adsorption of H<sub>2</sub>O and the corresponding independent gradient model based on Hirshfeld scatter plots, (f) Arrhenius plots from the proton conductivity versus temperature, (g)  $I_{\text{plateau}}$  vs.  $\omega^{1/2}$  linear fitting based on Levich equation, (h) Isotope experiments in D<sub>2</sub>O and H<sub>2</sub>O, (i) Zeta potential as the function of the time.



localize these electrons near imine N, pyridine N, and quinoline N,<sup>36, 37</sup> and the quantitative surface analysis in Figure 4b demonstrates that, compared with TTB-COF and BQ-TTB-COF, the electrostatic potential of QL-TTB-COF extends towards a more negative region. The introduction of lone pair electrons leads to a more negative electrostatic potential energy.<sup>38</sup> Therefore, in QL-TTB-COF, the introduced dipyrindyl and -COOH facilitate the binding of O<sub>2</sub> at the active dipyrindyl N sites.

Meanwhile, it is clear that the introduced dipyrindyl and -COOH improves the hydrophilicity of the COFs due to the much less water

contact angle (Figure 4c). The improved wettability enables rapid water penetration, ensuring the smooth proton transfer at the solid-liquid interface, which is a critical prerequisite for the subsequent PCET process.<sup>11, 17</sup> In addition, Figure 4d displays that TTB-COF, BQ-TTB-COF, and QL-TTB-COF exhibit distinct water vapor adsorption inflection points under relative pressure ( $P/P_0$ ), with the values at 0.62, 0.50 and 0.40, respectively. The low inflection point pressure of QL-TTB-COF indicates easy H<sub>2</sub>O cluster formation and smooth passage of H<sub>2</sub>O molecules in the pore channels via capillary effects.<sup>39</sup> Consequently, the introduction of -COOH promotes H<sub>2</sub>O molecules

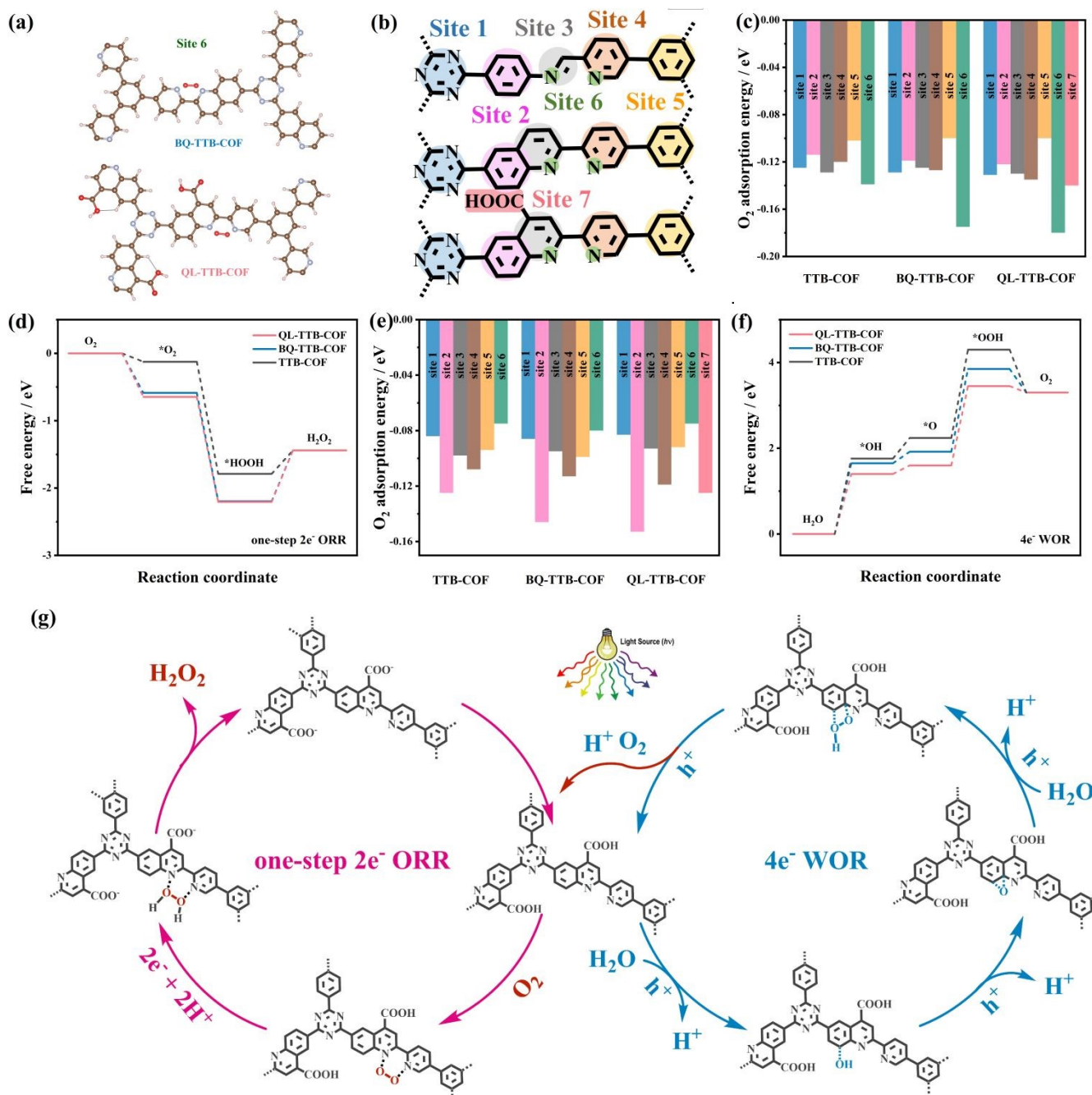


**Figure 5.** (a) O<sub>2</sub> adsorption sites and configuration on the COFs, (b) Potential O<sub>2</sub> adsorption sites of the COFs, (c) O<sub>2</sub> adsorption energy of the COFs, (d) Diagrams of free energies of one-step 2e<sup>-</sup> ORR, (e) H<sub>2</sub>O adsorption energy of the COFs, (f) Diagrams of free energies of 4e<sup>-</sup> WOR, (g) Possible reaction mechanism of the one-step 2e<sup>-</sup> ORR and 4e<sup>-</sup> WOR on QL-TTB-COF.



transfer in the pore channels, thereby enhancing proton transfer and O<sub>2</sub> utilization. In addition, strong capillary forces within the hydrophilic channels drive the rapid movement of water molecules, quickly transferring the generated H<sub>2</sub>O<sub>2</sub> into the bulk solution, thereby effectively preventing the secondary decomposition of H<sub>2</sub>O<sub>2</sub> at the reaction sites. Significantly, the possible mechanism of hydrogen-bond formation between the hydrogen atom of H<sub>2</sub>O and the oxygen atom of -COOH as H<sub>2</sub>O adsorption on QL-TTB-COF was systematically investigated using an independent gradient model based on Hirschfeld distribution analysis combined with scatter plot visualization (Figure 4e and Figure S44).<sup>40</sup> Furthermore, the real-space functional analysis characterized interaction strengths using key bond points derived from molecular atomic theory. It is noticeable that H<sub>2</sub>O molecules adsorbed on QL-TTB-COF exhibit more negative  $\lambda_2(\rho)$  and higher  $\delta_g$  at bond critical points compared to BQ-TTB-COF and TTB-COF.<sup>41</sup> This unique electronic structure implies much stronger interaction between -COOH and H<sub>2</sub>O in QL-TTB-COF.

To investigate the effect of -COOH on the proton conduction, the AC impedance spectroscopy was conducted at the temperature range of 303–353 K and 90% relative humidity (Figure S45). It can be seen that the proton conductivity rate of QL-TTB-COF ( $6.48 \times 10^{-2}$  S cm<sup>-1</sup>) is much greater than BQ-TTB-COF ( $1.16 \times 10^{-4}$  S cm<sup>-1</sup>) and TTB-COF ( $8.59 \times 10^{-4}$  S cm<sup>-1</sup>).<sup>17</sup> That is, introducing -COOH on the COFs really accelerates the proton conduction. In addition, the proton transfer activation energies ( $E_a$ ) of the three COFs were calculated using the temperature-dependent Arrhenius equation, yielding 0.25 eV, 0.34 eV and 0.36 eV, respectively (Figure 4f).<sup>11</sup> Of course, these  $E_a$  are all lower than 0.4 eV, indicating that the proton conduction follows the Grotthuss mechanism, where the H<sup>+</sup> are transferred in the hydrogen-bond networks.<sup>42</sup> Obviously, QL-TTB-COF owns the highest proton conductivity rate and the lowest  $E_a$  among the three COFs, and dense hydrogen-bond networks are readily formed in the pore channels, thereby accelerating the proton conduction in the frameworks. Moreover, the rotating disk electrode curves of the COFs were analyzed. Compared to BQ-TTB-COF and TTB-COF, QL-TTB-COF has the higher plateau current with all rotational speeds (Figure S23–S25), implying the increased proton density and the promoted proton transfer. This conclusion is further experimentally verified by the proton diffusion coefficient (D<sub>obs</sub>, H<sup>+</sup>), and Figure 4g shows that the H<sup>+</sup> in QL-TTB-COF is evidently greater than that in BQ-TTB-COF and TTB-COF.<sup>43</sup> It is noteworthy that the D<sub>obs</sub> and H<sup>+</sup> values discussed here reflect the overall influence of the photocatalysts on proton transfer at the electrode interface, rather than the absolute diffusion coefficient of H<sup>+</sup> in the solution.

Furthermore, the photocatalytic H<sub>2</sub>O<sub>2</sub> experiments were comparatively conducted in H<sub>2</sub>O and D<sub>2</sub>O. Figure 4h displays that compared to H<sub>2</sub>O, the activity of BQ-TTB-COF and TTB-COF in D<sub>2</sub>O decreases by 21% and 24%, respectively, while QL-TTB-COF remains almost unchanged. That is, the -COOH in QL-TTB-COF enhance the proton utilization. In addition, the solvent isotope effect (SIE), expressed as  $k_H/k_D$ , was determined for these photocatalysts.<sup>18</sup> Interestingly, the SIE values of BQ-TTB-COF and TTB-COF are within the range of 1.2 to 4, suggesting that the proton transfer is indeed the rate-determining step (RDS). In contrast, the SIE value of QL-TTB-COF is close to 1, indicating that the RDS does not involve the proton

transfer. In conclusion, the introduced dipyriddy in BQ-TTB-COF optimizes the thermodynamic O<sub>2</sub> adsorption, while the overall reaction rate is severely limited by the kinetically restricted proton transfer. Nevertheless, the hydrophilic pore channels in QL-TTB-COF by introducing -COOH overcomes the mass transfer barrier, making the proton transfer no longer the RDS. Moreover, the -COOH can ionize to release H<sup>+</sup>, and these H<sup>+</sup> can be quickly transferred to the active sites for the ORR at the initial stage. That is, the introduction of the -COOH on QL-TTB-COF achieves a perfect match between O<sub>2</sub> adsorption and PCET process, ensuring highly efficient H<sub>2</sub>O<sub>2</sub> production.

To verify the important role of H<sup>+</sup> in -COOH at the initial stage, the dynamic changes of the surface potential on the catalysts were investigated by monitoring the zeta potential (Figure 4i).<sup>38</sup> Under dark condition, no significant change is observed for the catalysts. After irradiation occurs, compared to BQ-TTB-COF and TTB-COF, the zeta potential of QL-TTB-COF exhibits a decreasing trend as O<sub>2</sub> is feed. This phenomenon is caused from the rapid deprotonation of -COOH, and the ionized H<sup>+</sup> acts as the “proton reservoir” and preferentially supplies H<sup>+</sup> to O<sub>2</sub> adsorbed at the dipyriddy N sites, thereby initiating the initial PCET process. As the irradiation time increases, its zeta potential distinctly rises, suggesting the H<sup>+</sup> on the surface is enriched by the WOR process. Subsequently, the H<sup>+</sup> is largely consumed in the ORR process, causing the zeta potential to decrease. As the photocatalysts are back to a dark environment, the zeta potential of QL-TTB-COF returns to be positive, demonstrating that the H<sup>+</sup> is accumulated. Additionally, the rate constant ( $K_f$ ) for H<sub>2</sub>O<sub>2</sub> generation was calculated during the first 12 min of the catalysis (Figure S46), it is evident that the  $K_f$  of QL-TTB-COF ( $2.05 \mu\text{mol g}^{-1} \text{h}^{-1}$ ) is significantly greater than BQ-TTB-COF ( $1.71 \mu\text{mol g}^{-1} \text{h}^{-1}$ ) and TTB-COF ( $1.49 \mu\text{mol g}^{-1} \text{h}^{-1}$ ). Noticeably, based on the independent gradient model derived from the Hirschfeld analysis, the dissociation enthalpy for proton release from -COOH and H<sub>2</sub>O oxidation was determined (Figure S47). It is clear that the dissociation enthalpy for proton release from -COOH ( $406 \text{ kJ mol}^{-1}$ ) is much less than that for H<sub>2</sub>O oxidation ( $500 \text{ kJ mol}^{-1}$ ).<sup>44</sup> That is, at the initial stage for H<sub>2</sub>O<sub>2</sub> production, the -COOH solves the problem of the delayed proton supply, supplying ample H<sup>+</sup> to accelerate the initial stage of the ORR by favorably initiating the PCET step. Subsequently, the ionized -COO<sup>-</sup> anions take the function of the proton relays, facilitating the proton transfer in the pore channels to ensure the efficient activation and conversion of O<sub>2</sub>.

The O<sub>2</sub> adsorption on the three COFs was thereafter carried out based on DFT calculations to understand the potential mechanism of the one-step 2e<sup>-</sup> ORR and the 4e<sup>-</sup> WOR process. The O<sub>2</sub> adsorption energies of the possible adsorption sites were initially calculated (Figure 5a and Figure S48–S53). As shown in Figure 5b, the triazine ring, benzene ring (1), C=N bond, pyridine ring, benzene ring (2), and the imine N and pyridine N, as well as -COOH are set as Site 1, 2, 3, 4, 5, 6 and 7, respectively. Among the three COFs, Site 6 has the greatest O<sub>2</sub> adsorption energy and is therefore selected as the reference. Notably, QL-TTB-COF has the greatest adsorption energy (-0.18 eV) at Site 6 (Figure 5c), significantly greater than BQ-TTB-COF (-0.17 eV) and TTB-COF (-0.13 eV). As shown in Figure 5d, the formation of the \*HOOH intermediate is the RDS in the one-step 2e<sup>-</sup> ORR pathway. The corresponding energy barriers for TTB-COF, BQ-



TTB-COF, and QL-TTB-COF are -2.83 eV, -1.61 eV and -1.59 eV, respectively. The lower energy barrier of QL-TTB-COF indicates that it more readily forms the intermediate \*HOOH, thereby promoting H<sub>2</sub>O<sub>2</sub> production.

For the 4e<sup>-</sup> WOR process, the H<sub>2</sub>O adsorption energies were calculated (Figure 5e). It is obvious that Site 2 exhibits the greatest H<sub>2</sub>O adsorption energy, with the values of -0.12 eV, -0.14 eV, and -0.15 eV for TTB-COF, BQ-TTB-COF, and QL-TTB-COF, respectively. In the 4e<sup>-</sup> WOR pathway (Figure 5f), the reaction from \*O to \*OOH is proven to be the RDS, with corresponding values of 2.06 eV, 1.93 eV, and 1.85 eV. These data confirm that QL-TTB-COF is more readily converted to O<sub>2</sub> via the 4e<sup>-</sup> WOR pathway. Therefore, a possible photocatalytic mechanism is proposed in Figure 5g. In the 2e<sup>-</sup> ORR process, the photo-generated electrons in QL-TTB-COF rapidly migrate to the active dipyridyl N sites, which act as the thermodynamically favorable sites to capture and activate O<sub>2</sub>. Benefiting from the localized proton environment established by the -COOH, the adsorbed O<sub>2</sub> undergoes a fast PCET process, it directly gains two e<sup>-</sup> and two H<sup>+</sup> from the adjacent -COOH to form \*HOOH intermediate, and further converts to H<sub>2</sub>O<sub>2</sub>. In the 4e<sup>-</sup> WOR process, the photo-generated holes first oxidize H<sub>2</sub>O to \*OH at Site 2, which is then dehydrogenated to \*O. Subsequently, another H<sub>2</sub>O undergoes similar dissociation process, forming a new \*OH. Ultimately, \*O and \*OH couple to produce O<sub>2</sub>, and simultaneously release abundant H<sup>+</sup>. Notably, the WOR process provides a continuous supply for the ORR. The released H<sup>+</sup> flows back by the hydrophilic channels to -COO<sup>-</sup>, thereby forming -COOH. The produced O<sub>2</sub> is captured again by dipyridyl N, thus establishing a perfect closed-loop system. This dynamic synergy between O<sub>2</sub> adsorption and PCET process fundamentally ensures efficient and sustained operation of photocatalytic H<sub>2</sub>O<sub>2</sub> production.

## Conclusions

In summary, we developed a dual synergistic regulation strategy of COF photocatalysts targeting strong O<sub>2</sub> adsorption and rapid PCET process for H<sub>2</sub>O<sub>2</sub> production. The synthesized COF photocatalyst, QL-TTB-COF, enables precise control of the photocatalytic microprocesses: At the thermodynamic level, the introduced highly stable quinoline rings reshape the local electronic structure at the active dipyridyl N sites, effectively overcoming the deficiency of insufficient electron affinity and hence enhancing Yeager-type side adsorption of O<sub>2</sub>. At the kinetic level, the introduced -COOH improves the hydrophilicity of the pore channels, and more critically, it serves as the proton source in the initial ORR, which substantially lowers the energy barrier and establishes efficient proton transfer networks. Particularly, this ingenious regulation triggers the 4e<sup>-</sup> WOR pathway. Through this synergistic "O<sub>2</sub> adsorption enhancement-proton pump acceleration" mechanism, QL-TTB-COF achieves an exceptionally high H<sub>2</sub>O<sub>2</sub> yield rate of 7848 μmol g<sup>-1</sup> h<sup>-1</sup> (AQY=8.8%). This work provides a novel paradigm to precisely regulate the thermodynamic O<sub>2</sub> adsorption and the kinetic proton transfer process for efficient photocatalytic H<sub>2</sub>O<sub>2</sub> production, and it also establishes a facile strategy for the rational construction of highly efficient COF photocatalysts.

## Author contributions

Hao Wang: conceptualization, formal analysis, investigation, resources, data curation and writing. Junjiang Zong: methodology, formal analysis, investigation and resources. Shiyuan Wei: methodology and investigation. Meng Li: methodology and investigation. Lingfeng Zhu: methodology and investigation. Xiaodong Sun: methodology and investigation. Liquan Ye: methodology and investigation. Jianhan Huang: conceptualization, supervision, review & editing and project administration. Jiawei Li: conceptualization and supervision. You-Nian Liu: supervision and project administration. Tianyi Ma: supervision and project administration.

## Conflicts of interest

There are no conflicts to declare.

## Data availability

The data supporting this article have been included as part of the supplementary information (SI). Supplementary information is available.

## Acknowledgements

The National Natural Science Foundation of China (Nos. 22478442 and 22308389) and the 111 Project (D20015) were acknowledged for the financial supports.

## Notes and references

1. B. Lin, D.-H. Si, J.-J. Li, S.-Y. Gao, X. Yang and R. Cao, *Adv. Mater.*, 2026, **38**, e20022.
2. J. Chen, S. Yan, F. Wang, F. Lin, J. Lin, R. A. Borse and Y. Wang, *Angew. Chem. Int. Ed.*, 2025, **64**, e202500924.
3. L. Li, X. Lv, Y. Xue, H. Shao, G. Zheng and Q. Han, *Angew. Chem. Int. Ed.*, 2024, **63**, e202320218.
4. H. Zhang, R. Ma, K. Chi, Y. Liu and Y. Zhao, *Angew. Chem. Int. Ed.*, 2025, **64**, e202516657.
5. A. Chakraborty, A. Alam, U. Pal, A. Sinha, S. Das, T. Saha-Dasgupta and P. Pachfule, *Nat. Commun.*, 2025, **16**, 503.
6. T. Xu, Z. Wang, W. Zhang, S. An, L. Wei, S. Guo, Y. Huang, S. Jiang, M. Zhu, Y.-B. Zhang and W.-H. Zhu, *J. Am. Chem. Soc.*, 2024, **146**, 20107-20115.
7. J. Cheng, Y. Wu, W. Zhang, L. Wang, X. Wu and H. Xu, *Adv. Mater.*, 2025, **37**, 2410247.
8. Z. Chen, H. Weng, C. Chu, D. Yao, Q. Li, C. Zhang and S. Mao, *Nat. Commun.*, 2025, **16**, 6943.
9. C. Sun, Y. Han, H. Guo, R. Zhao, Y. Liu, Z. Lin, Z. Xiao, Z. Sun, M. Luo and S. Guo, *Adv. Mater.*, 2025, **37**, 2502990.
10. T.-X. Luan, Q. Wei, C. Xin, S. Y. Wong, Y. Li, Y. Zheng, Y. Li, G. Liu, W. W. Yu, X. J. Loh, X. Li and P.-Z. Li, *Adv. Mater.*, 2026, **38**, e15517.
11. K. Yang, L. Chen, K. Xiong, J. Yang, M. Adeli, S. Li, M. Wang, C. Cheng and C. Zhao, *Adv. Funct. Mater.*, 2025, **36**, e20900.
12. G. Chakraborty, P. Das, B. Bhattacharya, C. Prinz, F. Emmerling and A. Thomas, *Chem. Sci.*, 2026, **17**, 4107-4115.



13. Y. Lin, J. Zou, X. Wu, S. Tong, Q. Niu, S. He, S. Luo and C. Yang, *Nano Lett.*, 2024, **24**, 6302-6311.
14. N. Mu, Z. Luo, W. Shan, H. Huang and H. Tang, *ACS Sustainable Chem. Eng.*, 2025, **13**, 16534-16543.
15. X. Ma, H. Pan, L. Gong, X. Ding, X. Zhou, H. Liu, R. Wang, C. Qu, Y. Zhao, D. Qi, Y. Bian and J. Jiang, *Angew. Chem. Int. Ed.*, 2025, **64**, e202511024.
16. D. Chen, W. Chen, Y. Wu, L. Wang, X. Wu, H. Xu and L. Chen, *Angew. Chem. Int. Ed.*, 2023, **62**, e202217479.
17. T.-X. Luan, Q. Wei, C. Xin, S. Y. Wong, Y. Li, Y. Zheng, Y. Li, G. Liu, W. W. Yu, X. J. Loh, X. Li and P.-Z. Li, *Adv. Mater.*, 2025, **38**, e15517.
18. C. Liu, X. Liu, B. Chen, Z. Li, X. Ou, Y. Lu, Y. Liu, C. Wu, S. Yao, Y. Liu, L. Ye, B. Han and Z. Yang, *Nat. Commun.*, 2025, **16**, 8941.
19. P. Huang, Y.-Y. Peng, X.-H. Wang, R.-H. Li, M.-H. Qin, M. Zhang, S.-M. Wang, M. Lu, S.-L. Li and Y.-Q. Lan, *Adv. Mater.*, 2026, **38**, e07849.
20. Z. Luo, X. Chen, W. Yang, Y. Chang, S. Zhu, F. Zhang, W. Lin, G. Xu, G.-E. Wang and X. Chen, *Sci. China Chem.*, 2025, **68**, 6639-6647.
21. D. Chen, W. Chen, G. Zhang, S. Li, W. Chen, G. Xing and L. Chen, *ACS Catal.*, 2022, **12**, 616-623.
22. W. Wu, Z. Li, S. Liu, D. Zhang, B. Cai, Y. Liang, M. Wu, Y. Liao and X. Zhao, *Angew. Chem. Int. Ed.*, 2024, **63**, e202404563.
23. K.-H. Xie, G.-B. Wang, F. Huang, F. Zhao, J.-L. Kan, Z.-Z. Chen, L. Cai, S.-L. Han, Y. Geng and Y.-B. Dong, *Nat. Commun.*, 2025, **16**, 3493.
24. P. Das, G. Chakraborty, J. Roeser, S. Vogl, J. Rabeah and A. Thomas, *J. Am. Chem. Soc.*, 2023, **145**, 2975-2984.
25. Y. Yang, L. Yu, T. Chu, H. Niu, J. Wang and Y. Cai, *Nat. Commun.*, 2022, **13**, 2615.
26. R. Wang, I. Nath, J. Chakraborty, L. Wang and P. Van Der Voort, *J. Mater. Chem. A*, 2025, **13**, 36375-36381.
27. Y. Zhang, Y. Liu, H. Li, G. Bai and X. Lan, *Chem. Eng. J.*, 2024, **489**, 151479.
28. N.-F. Wan, Y.-Q. Wang, L. Fu, J. Liu, B. A. Woodcock, Y.-Q. Hu, A. Eskelinen, A. Hector, M. Loreau, Y. Hautier, R. D. Bardgett, P. Kardol, D. Zuppinger-Dingley, L. H. Fraser, J. M. Bullock, S. Nakagawa, S. Shen, F. Xin, D.-P. Shi, Z. Li, J. Zhou and C. Scherber, *Nat Ecol Evol*, 2026, **10**, 293-307.
29. Y. Ju, H. Lin, G. Tan, P. Su, Z. Wang, C. Hu, R. Hou, T. Hao, F. Chen and Y. Tang, *Nat. Commun.*, 2025, **16**, 5658.
30. C. Qin, X. Wu, L. Tang, X. Chen, M. Li, Y. Mou, B. Su, S. Wang, C. Feng, J. Liu, X. Yuan, Y. Zhao and H. Wang, *Nat. Commun.*, 2023, **14**, 5238.
31. Y. Luo, B. Zhang, C. Liu, D. Xia, X. Ou, Y. Cai, Y. Zhou, J. Jiang and B. Han, *Angew. Chem. Int. Ed.*, 2023, **62**, e202305355.
32. H. Wang, F. Zhou, S. Wei, M. Li, J. Li, J. Huang and Y.-N. Liu, *Appl. Catal. B Environ.*, 2026, **384**, 126234.
33. Q. Nan, J. Ning, B. Han, H. Wei, X. Wang, Y.-Y. Gu, S. Zhou, G. Cao, G. Zhang, X. Li, Y. Jia and L. Hao, *Chem. Sci.*, 2026, **17**, 466-474.
34. H. Xu, Y. Wang, Y. Xu, Q. Wang, M. Zhuang, Q. Liao and K. Xi, *Angew. Chem. Int. Ed.*, 2024, **63**, e202408802.
35. F. Hao, C. Yang, X. Lv, F. Chen, S. Wang, G. Zheng and Q. Han, *Angew. Chem. Int. Ed.*, 2023, **62**, e202315456.
36. T. Lu and S. Manzetti, *Struct. Chem.*, 2014, **25**, 1521-1533.
37. S. Manzetti and T. Lu, *J. Phys. Org. Chem.*, 2013, **26**, 473-483.
38. X. Sun, Y. Dong, T. Yang, Y. Ling, H. Zhao, J. Zhang and Y. Zhu, *Angew. Chem. Int. Ed.*, 2025, **65**, e24222.
39. Y. Chen, R. Liu, Y. Guo, G. Wu, T. C. Sum, S. W. Yang and D. Jiang, *Nat. Synth.*, 2024, **3**, 998-1010.
40. T. Lu and Q. Chen, *J. Comput. Chem.*, 2022, **43**, 539-555.
41. H. Cheng, Z. Ma, P. Kumar, H. Liang, Z. Cao, H. Xie, L. Cavallo, H. Kim, Q. Li, Y.-K. Sun and J. Ming, *Adv. Energy Mater.*, 2024, **14**, 2304321.
42. A. Yu, W. Liu, W. Xi, M. Mu and L. Shi, *Chem. Mater.*, 2024, **36**, 1880-1890.
43. H. Ooka, M. C. Figueiredo and M. T. M. Koper, *Langmuir*, 2017, **33**, 9307-9313.
44. H. Li, Y. Li, X. Lv, C. Liu, N. Zhang, J. Zang, P. Yue, Y. Gao, C. Liu and Y. Li, *Adv. Mater.*, 2025, **37**, 2415126.



**Data Availability statement:**

The authors declare that the data supporting the findings of this study are available within the paper and its Supplementary Information files.

